

Simple fabrication of an uncooled Al/SiO₂ microcantilever IR detector based on bulk micromachining

Hassan Abdollahi · Hassan Hajghassem ·
Shams Mohajerzadeh

Received: 22 March 2013 / Accepted: 7 June 2013 / Published online: 19 June 2013
© Springer-Verlag Berlin Heidelberg 2013

Abstract A simple microfabrication process to make an uncooled aluminum/silicon dioxide bi-material microcantilever infrared (IR) detector using silicon bulk micromachining technology is presented in this work. This detector is based on high banding of the microcantilever due to the large dissimilar in thermal expansion coefficients between the two materials. It consists of a 1 μm SiO₂ layer deposited by 200 nm thin Al layer. Since no sacrificial layer is used in this process, complexity related to releasing sacrificial layer is avoided. Moreover Al is protected in Si etchant using dual-doped tetramethyl ammonium hydroxide. The other advantage of this process is that only three masks are used with four photolithography process. Thermal and thermal mechanical behaviors of this structure are obtained using finite element analysis, and the maximum temperature and displacement at the end of cantilever at 100 pW/μm² absorbed IR power density on top surface are 7.82°K and 1.924 μm, respectively.

Abbreviations

FEA	Finite element analysis
IR	Infrared
TMAH	Tetramethyl ammonium hydroxide
MEMS	Micro electromechanical system

H. Abdollahi (✉) · H. Hajghassem
Department of Electrical Engineering, Science and Research
Branch, Islamic Azad University, Tehran, Iran
e-mail: hassan_abdollahi@yahoo.com

S. Mohajerzadeh
Nano-Electronic Center of Excellence, Nano-Electronic and
Thin Film Laboratory, University of Tehran, Tehran, Iran

S. Mohajerzadeh
Department of Electrical and Computer Engineering,
University of Tehran, Tehran, Iran

SEM	Scanning electron microscope
CTE	Thermal expansion coefficients
Al	Aluminum
Au	Gold
BOE	Buffered hydrofluoric acid
Cr	Chromium
DI	De-ionized
HF	Hydrofluoric acid
Si	Silicon
SiN _x	Silicon nitride
SiO ₂	Silicon dioxide
A	Cross-section area of leg
A _{ab}	IR absorbed area
L	One of the folded lengths of leg
t ₁	Thickness of Al layer
t ₂	Thickness of SiO ₂ layer
T	Element temperature
ΔT	Temperature rise
ΔT _s	Blackbody target temperature change
G _{Total}	Total thermal conduction between the detector structure and the surroundings regain
G _{air}	Air thermal conductance
G _{rad}	Thermal radiative conductance
G _{leg}	Thermal leg's conductance
V	Volume of film
W _s	Absorbed IR power density
n	Ratio of Al and SiO ₂ Young's modulus
x	Al and SiO ₂ thickness ratio
c	Heat capacity
σ	Stefan–Boltzmann constant
ρ	Density of the material
ε _{Al}	Al emissivity
ε _{SiO₂}	SiO ₂ emissivity
k	Thermal conductivity coefficient

η	IR absorption efficiency
τ_0	Optical transmission efficiency
F	f number of the optics
$(dP/dT)_{\lambda_1-\lambda_2}$	IR target power emission rate per unit area within 8–14 μm wavelength range
α_1	CTE of Al layer
α_2	CTE of SiO_2 layer

1 Introduction

Infrared detectors are widely used in industrial (Vigni and Cocchi 2013), commercial (Correa et al. 2012), security surveillance (Zhu et al. 2013), medical (Oh et al. 2012) and military applications (Gray et al. 2013). Photon detectors and thermal detectors are two types of IR detectors in 8–12 μm range. High sensitive photo detectors require large and high cost cooling system to reduce temperature about 70 K at acceptable thermal noise level (Razeghi et al. 2013; Kruse 1995). Thermal IR detectors generate heat by absorbing IR radiation (Wang et al. 2013). Many different kinds of these detectors have been studied and suggested, and researchers have been recently driven toward uncooled micro electromechanical system (MEMS) IR detector due to their simplicity, low cost and working at the ambient temperature. Pyroelectrics (Xu et al. 2012; Fujitsuka et al. 1998), Thermopiles (Szentpali et al. 2012; Schieferdecker et al. 1995), Bolometers (Wang et al. 2012; Dobrzanski et al. 1997) and Microcantilevers (Cheng et al. 2013a) are among these types of uncooled detectors.

In the past years, suspended micromechanical IR detectors structures have been introduced by using a bi-material effect in MEMS technologies, since they don't need electrical wiring to suspend structure. Moreover these kinds of detectors have low noise characteristic and high sensitivity due to the absence of shot noise and higher thermal isolation (Cheng et al. 2013a). The basic function of this detector depends on the bi-material microcantilever deformation due to mismatch of thermal expansion coefficients between two different materials by absorption of IR energy. Bending can simply be measured by using piezoresistive (Li et al. 2011), optical (Cheng et al. 2009), or capacitive methods (Cao et al. 2009). Gold/silicon nitride (Au/SiN_x) structure using low chemical vapor deposition is the basic structure which is widely used by most of the researchers, due to its high uniformity and compatibility with silicon processing (Zhao et al. 2012; Cheng et al. 2013b).

SiO_2 has lower thermal conductivity and lower coefficient of thermal expansion compare to SiN_x . On the other hand, Al has larger thermal expansion coefficient than Au. As a result, Al/SiO_2 structure is more suitable than $\text{Au}/$

SiN_x , Al/SiN_x and Au/SiO_2 structures for IR detection (Kwon et al. 2007; Grbovic et al. 2008a).

High sensitivity in cantilever displacement due to variation in temperature in Al/SiO_2 structures makes it a good candidate for microcantilever IR detector. However, high stress and incompatibility with KOH, EDP and TMAH silicon etchant are the biggest challenge to construct Al/SiO_2 structure using bulk micromachining technique (Biswas et al. 2006).

Recently, Hunter and Maurer (2006, 2007) and Kwon et al. (2007, 2008, 2009) introduced Al/SiO_2 structure by using surface micromachining with sacrificial layer technique. On the other hand, Grbovic et al. (2008a, b, 2009) introduced other Al/SiO_2 structure using bulk micromachining technology with $\text{CHF}_3\text{-O}_2$ deep reactive ion etching process. They improved micromechanical IR detectors performance and proved the possibility of its process fabrication.

The aim of this paper is to investigate the feasibility of fabricating suspend Al/SiO_2 uncooled bi-material IR detector using a simple fabrication process based on silicon bulk micromachining technique with wet releasing process.

2 Detector operation

The IR bi-material microcantilever detector consists of two thin films which are deposited, etched and released to construct the willing form with MEMS technologies. The two chosen materials must meet following basic requirement: (Su and Duan 2011; Dong et al. 2007; Li 2004).

- (1) The IR radiation in the range of 8–14 μm should be absorbed by one of the two materials, and the other material should have a high IR reflection coefficient;
- (2) The difference of mismatch in thermal expansion coefficients between the two materials should be maximized;
- (3) One of the layers should have low thermal conductivity;
- (4) Both materials should have a similar Young's module;
- (5) Silicon etchant must not affect the two materials.

In this work, SiO_2 and Al layer are selected to form bi-material cantilever structure. SiO_2 can be used to absorb IR radiation in the 8–14 μm range. Physical properties of SiO_2 and Al are compared to SiN_x and Au as shown in Table 1. As it can be seen in this table, CTE of SiO_2 and Al are 0.41×10^{-6} and $23.1 \times 10^{-6} \text{ K}^{-1}$, respectively. When the IR radiation is absorbed in Al/SiO_2 structure, large bending of microcantilever is formed compared to Si_3N_4 and Au structure due to higher mismatch of CTE between SiO_2 and Al. On the other hand, thermal conductivity of

Table 1 Material property of Si₃N₄, SiO₂, Al and Au (Weidong Wang et al. 2006)

Material	Si ₃ N ₄	SiO ₂	Al	Au
Young’s modulus (MPa)	130 × 10 ³	70 × 10 ³	70 × 10 ³	78 × 10 ³
Poisson ratio	0.25	0.25	0.35	0.44
Coefficient of thermal expansion (/K)	1.6 × 10 ⁻⁶	0.41 × 10 ⁻⁶	23.1 × 10 ⁻⁶	14.2 × 10 ⁻⁶
Thermal conductivity (pW/μm K)	2.9 × 10 ⁷	1.1 × 10 ⁶	2.35 × 10 ⁸	3.23 × 10 ⁸
Density (kg/μm ³)	2.6 × 10 ⁻¹⁵	2.3 × 10 ⁻¹⁵	2.7 × 10 ⁻¹⁵	1.93 × 10 ⁻¹⁴
Specific heat (pJ/kg K)	6.9 × 10 ¹⁴	16.6 × 10 ¹⁴	8.97 × 10 ¹⁴	1.29 × 10 ¹⁴

SiO₂ (i.e. 1.1 × 10⁶ pW/μm K) is lower than Si₃N₄ (i.e. 2.9 × 10⁷ pW/μm K), which helps to increase the thermal displacement in cantilever.

Of course, thermal conductivity and expansion coefficient of polymers make them the ideal materials to construct IR microcantilever detector. However they suffer from high natural stresses (Zhao et al. 2002).

Figure 1 shows the schematic diagram of a top view of the designed uncooled IR microcantilever detector pixel structure. One end of microcantilever is fixed mechanically and the other end is free to move with any changes in force or stress. The pixel structure is divided to four important elements: main frame, an IR absorber/deformation structure, two bi-materials bending legs and two thermal isolation legs. The operation of this detector is as follow:

- (1) Main frame of SiO₂ is used as a supporting structure for the detectors.
- (2) The IR absorber area (100 × 70 μm) is composed of SiO₂ and an Al layer. To increase the absorption of IR energy no etching hole is considered for this area.

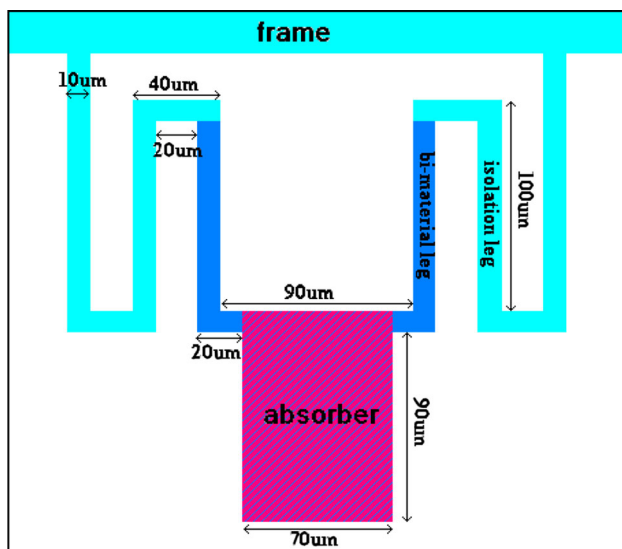


Fig. 1 Schematic diagram of a top view of the uncooled IR microcantilever detector with three-folded legs structure. Absorber red area is 100 × 70 μm², and blue bi-material legs length and total bluish thermal isolation legs length with 10 μm width are 90 and 270 μm, respectively

Due to the reflection of the incident IR flux by thin Al mirror in the absorber, the absorption of IR radiations is increased. The IR absorber also includes the bi-material structure to increase the thermo-mechanical bending.

- (3) The two bi-materials legs (90 × 10 μm each) also consist of SiO₂ and Al layers with the same IR absorber connecting to IR absorber. Heat produced from the IR absorber is directly conducted to the bi-material arms due to temperature difference between them. Then the arms and the IR absorber simultaneously bend by bi-material effect owing to the differential stress in the large mismatch CTE between bi-layers. The detector displacement can be maximized due to elongation of the bi-material region extended to the IR absorber area. Hence, the heat energy is converted to mechanical displacement. This bending can consequently be measured by readout system.
- (4) The two-fold thermal isolation support legs (90 × 10 μm each) as shown in Fig. 1. It consists of SiO₂ layer which is connected to bi-material legs. Due to the high thermal resistivity of SiO₂ and increasing the total length of legs, this isolation legs reduce the heat convection from bi-material area to main frame. As a result the detector temperature is increased and so more displacement of bi-material leg is achieved.

3 Thermal and thermomechanical analysis

The free end of bi-material legs is bended due to large differences between CTE values. Thermodynamic analysis can be given the relation between detector displacement, ΔZ and temperature variation of sensitive area, ΔT as follow (Datskos et al. 2004):

$$\Delta Z = (3L^2/t_2) \times (\alpha_1 - \alpha_2) \times \Delta T \times K(m) \tag{1}$$

where L is the length of the bi-material parts, t₁ is the thickness of Al layer, α₁ and α₂ are CTE of Al and SiO₂ layers, respectively, and K is introduced by the following equation (Datskos et al. 2004):

$$K = (1 + x)/(4 + 6x + 4x^2 + nx^3 + 1/nx) \tag{2}$$

Here $x = t_1/t_2$ is the ratio between Al and SiO₂ thicknesses and $n = E_1/E_2$ is the ratio of Al and SiO₂ Young’s modulus. To obtain displacement of the detector, the variation of detector temperature due to absorbed IR power flux should be calculated.

The detector temperature is analyzed when the detector is in thermal equilibrium with surroundings area. The ΔT can be expressed by the heat flow equation (Kruse 1996).

$$C \frac{d(\Delta T)}{dt} + G_{Total}(\Delta T) = \eta P = W_s \times A_{ab} \tag{3}$$

where, C is the heat capacity of pixel sensitive area, G_{Total} is the total thermal conduction between the detector structure and the surroundings region, P is the incident power on the pixel, η is the absorption efficiency, W_s is the absorbed IR density and A_{ab} is IR absorbed area. In this equation, the heat capacity of pixel sensitive area is $C = \rho.V.c$ in which, ρ is the density of the material, V is the volume of the film and c is the specific heat capacity (Jiao et al. 2006). The temperature rise ΔT can approximately be calculated along the bi-material region by using Eq. (3) considering uniform temperature distribution assumption (Paul W. Kruse 1996):

$$\Delta T = \frac{W_s \times A_{ab}}{G_{Total}} (^{\circ}C) \tag{4}$$

W_s is the absorbed IR density on the detector and can be expressed as (Wang et al. 2006):

$$W_s = \eta \tau_0 \frac{1}{4F^2} \left(\frac{dP}{dT} \right)_{\lambda_1-\lambda_2} \times \Delta T_s (W/m^2) \tag{5}$$

In which η is IR absorption efficiency, τ_0 is optical transmission efficiency, F is f number of the optics, $(dP/dT)_{\lambda_1-\lambda_2}$ is the IR target power emission rate per unit area within 8–14 μm wavelength range at 300°K and ΔT_s is the

Table 2 Theoretical calculation parameters

Thermal radiative conductance G_{rad} (W/K)	3.39×10^{-8}
Thermal leg’s conductance G_{leg} (W/K)	8.06×10^{-8}
Total thermal conductance G_{Total} (W/K)	1.14×10^{-7}
Air thermal conductance in a vacuum chamber (W/K)	$\sim 10^{-10}$
Temperature variation ΔT (°K)	6.15
Bi-material microcantilever deflection ΔZ (μm)	1.75
Absorbed IR power density W_s (pW/ μm^2)	100.215
IR target power emission rate in 8–14 μm wavelength range	2.62
Element temperature T (°K)	298
Blackbody target temperature change ΔT_s (°K)	340
IR absorption efficiency η	0.9
Optical transmission efficiency τ_0	0.5
f number of the optics F	1.0

blackbody target temperature change. The value used for η , τ_0 , ΔT_s , $(dP/dT)_{\lambda_1-\lambda_2}$, and f is shown in Table 2.

The maximum temperature of detector is obtained when the G_{Total} is minimized to its lowest value. The G_{Total} is composed of three independent main parts (Zhao 2002): the air thermal conductance G_{air} , the thermal radiative conductance G_{rad} and the thermal leg’s conductance G_{leg} .

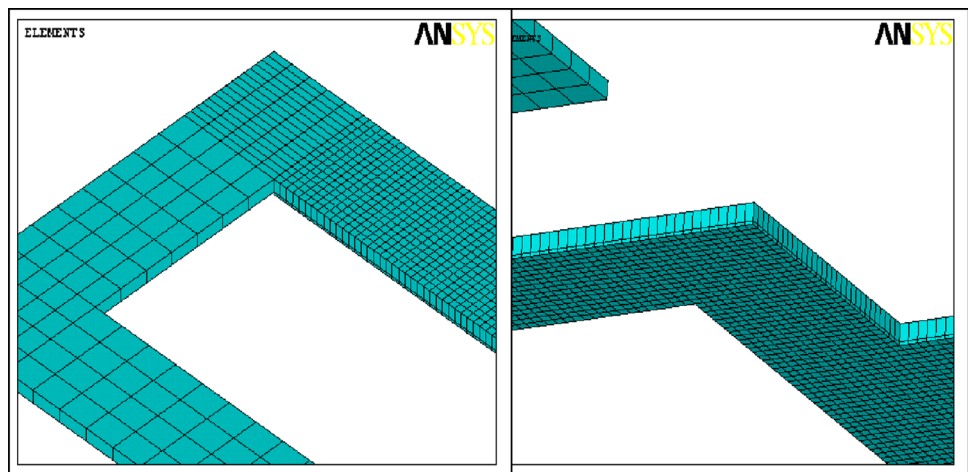
$$G_{Total} = G_{air} + G_{rad} + G_{leg} (W/K) \tag{6}$$

where the air thermal conductance G_{air} is approximately 10^{-10} W/K in vacuum chamber (Datskos et al. 2004). Since this value is much lower than G_{Total} (1.14×10^{-7} W/K), this term can be eliminated. So Eq. (6) can be rewritten as:

$$G_{Total} = G_{rad} + G_{leg} (W/K) \tag{7}$$

G_{rad} is the thermal conductance of radiation between the detector and its environments, which is given as (Datskos et al. 2004):

Fig. 2 The meshed model of the microcantilever IR detector is shown in two regions with step by step increasing element size. Ratio dimensions between vertical and horizontal are 4 to 1



$$G_{rad} = 4\sigma \times A_{ab} \times (\epsilon_{Al} + \epsilon_{SiO_2}) \times T^3 (W/K) \tag{8}$$

In which σ is the Stefan–Boltzmann constant ($5.67 \times 10^{-8} \text{ Wm}^{-2} \text{ K}^{-4}$), ϵ_{Al} (0.01) and ϵ_{SiO_2} (0.781) are Al and SiO_2 emissivity, respectively, and T is the element temperature ($\sim 298^\circ\text{K}$). The calculated value for G_{rad} is $3.39 \times 10^{-8} \text{ W/K}$. G_{leg} is the thermal leg’s conductance between the detector and the substrate, and can be calculated from:

$$G_{legl} = \left[\frac{1}{2} \left(\frac{L}{A_{SiO_2} \times k_{SiO_2} + A_{Al} \times k_{Al}} \right) + \left(\frac{L}{A_{SiO_2} \times k_{SiO_2}} \right) \right]^{-1} (W/K) \tag{9}$$

where k_{SiO_2} and k_{Al} are the thermal conductivity coefficient of the SiO_2 and Al legs material, respectively, A_{SiO_2} and A_{Al} are the cross-section areas of the SiO_2 and Al legs, respectively and L is one of the folded lengths of the legs. The calculated value for G_{leg} is $8.06 \times 10^{-8} \text{ W/K}$. It is obvious that a low k material and longer thermal isolation legs with a small cross section area is needed to reduce G_{leg} . Calculation parameters of this design are shown in Table 2.

4 Simulation

The thermal and thermal–mechanical behaviors of the microcantilever detector are modeled and simulated using ANSYS finite element analysis software. The maximum temperature change of the detector and temperature distributions of the device under an applied IR power density are simulated by using *Brick 20Node 90* thermal solid element. Then, the maximum mechanical deformation of the cantilever system under temperature change is simulated by using *SOLID95* thermal-structural element (Wang et al. 2006).

A meshed model is shown in Fig. 2. Al layer thickness is chosen on a smaller solid element size in vertical dimension. The ratio dimensions between vertical and horizontal is chosen as 4 to 1, to trade off between simulation accuracy and calculation time. The element size is also increased step by step to reduce the calculation time.

The movement and the temperature at the end of isolation legs are set at 0 and 25°C , respectively. Constant heat flux is set at $100 \text{ pW}/\mu\text{m}^2$ under the IR absorption on the top surface of the plate as boundary conditions, and air conduction and convection heat loss are ignored. The thermal and mechanical properties of some material used for bi-material cantilever and details of the detector dimensions used in FEA simulations are provided in Tables 1 and 3, respectively.

Table 3 Dimensions of the uncooled IR detector

Structure	Material	Dimension (μm)
IR absorber area	SiO_2/Al	100×70
Absorber and isolation layer thickness	SiO_2	1
Metal layer thickness	Al	0.2
Bi-materials leg’s length	SiO_2/Al	90
Bi-materials leg’s width		10
One Isolation leg’s length	Al	100
Isolation leg’s width		10

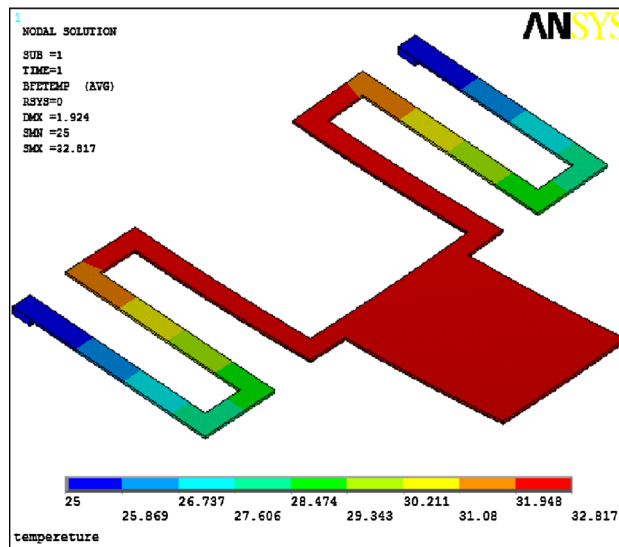


Fig. 3 FEM simulation result of 7.82°K temperature variation distributions under incident radiation of $100 \text{ pW}/\mu\text{m}^2$ on top of surface the plate

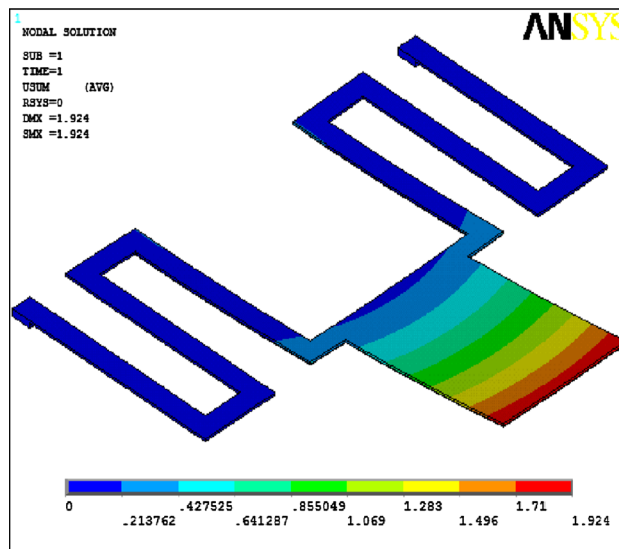


Fig. 4 FEM simulation result of $1.924 \mu\text{m}$ maximum deflection of the detector due to temperature variation of Fig. 3

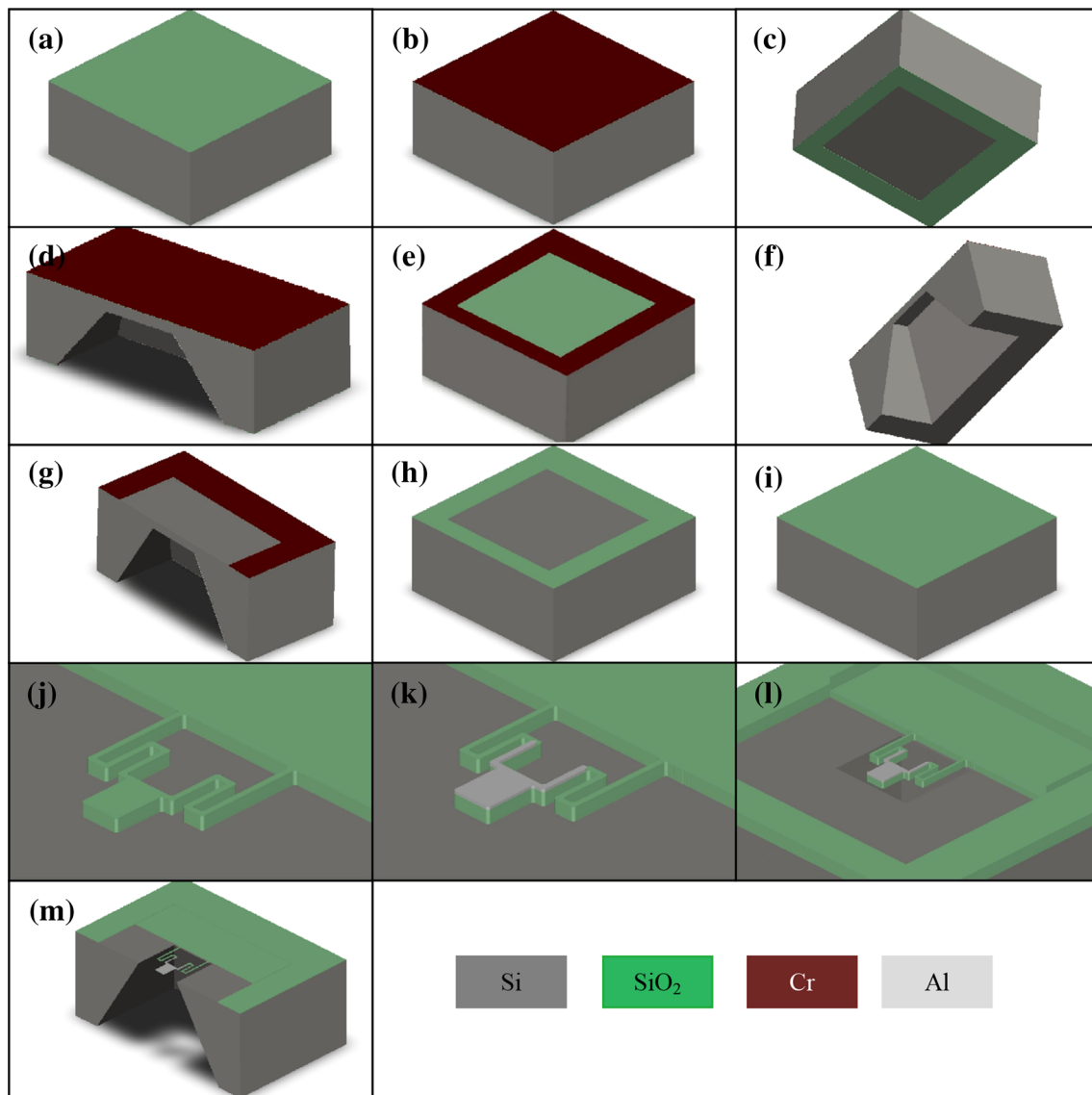


Fig. 5 Fabrication process of the microcantilever-based IR detector: **a** growing of the 2 μm thick SiO_2 mask layer on the substrate, **b** evaporation of the 400 nm thick Cr mask layer on the SiO_2 in *front side*, **c** patterning of *backside* SiO_2 layer by BOE etchant, **d** etching of Si using TMAH etchant to make 60 μm thin membrane, **e** double-side lithography technique used to pattern in *front side* Cr layer, **f** continuing the silicon etching again to observe *red* thin film

membrane, **g** removing of SiO_2 layer using BOE etchant, **h** removing Cr layer completely, **i** growing 1 μm thick SiO_2 basic structure layer on *front-side*, **j** patterning of in *front side* SiO_2 layer, **k** evaporation of 200 nm thick Al film on *front-side* and patterned by lift-off process, **l** removing of residual Si with dual-doped TMAH and **m** release of the structure using a low temperature wet releasing process

Figure 3 shows the temperature simulation result. As it is shown in this Figure, the maximum temperature difference between the detector and its substrate is about 7.82°K. This value is in agreement with the calculation. This figure also shows that distribution of the temperature linearly decreases on thermal isolation arms; and is nearly uniform on bi-material arms and IR absorber due to higher thermal conductivity of Al compare to SiO_2 . The simulated result of the detector deflection is shown in Fig. 4, as it is shown in this Figure, the maximum bending is about 1.924 nm.

This value is in agreement with the calculation results. It also shows that the SiO_2 isolation arms are not bended.

5 Microfabrication process

Comparing to the pervious reported works on SiO_2/Al bi-material cantilever (Hunter and Maurer 2006, 2007; Kwon et al. 2007, 2008, 2009; Grbovic et al. 2008a, b, 2009), the presented microfabrication process in this work is

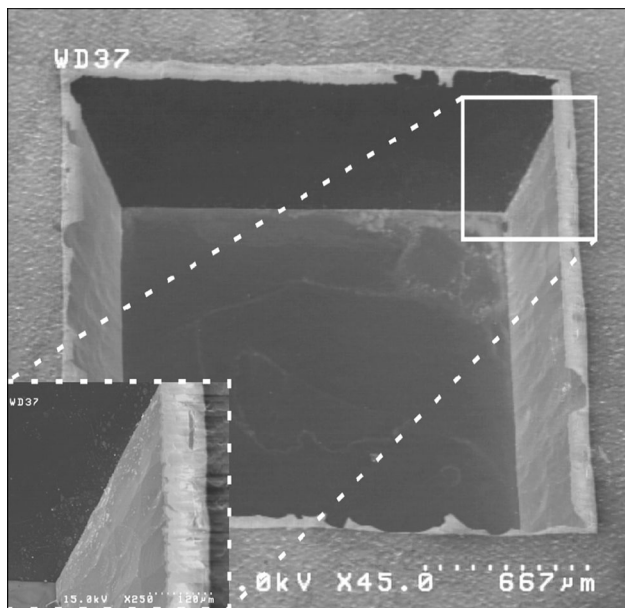


Fig. 6 SEM image of *back side* membrane

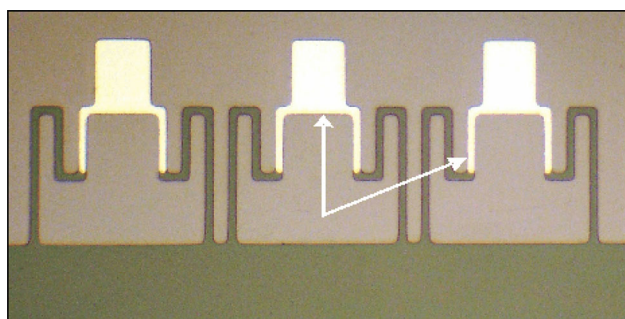


Fig. 7 Optical image of Al patterning. *Arrows* show the presence of two different layers in the side-bars

simplified by avoiding the sacrificial layer process by means of using silicon bulk micromachining technologies and a wet releasing process. Fabrication of the implemented IR uncooled detector involves four photolithographic processes with 3 masks. The microfabrication process typically consists of thirteen steps: growing of the SiO₂ layer on the substrate, evaporation of the chromium (Cr) film in front side, patterning of backside SiO₂ layer, etching of silicon, patterning the front side Cr layer, repeating the Si etching, removing of SiO₂ layer, removing Cr layer, growing a new SiO₂ on the substrate, patterning of front side SiO₂ layer, evaporation of the Al film and liftoff, removing of the residual Si with dual-doped TMAH and releasing of the structure.

Figure 5 shows the basic fabrication steps used to implement the simple microfabrication IR uncooled detector in this work. 485 µm thick single-side-polished p-type (100) silicon wafer is used in this process. The wafer is cleaned by RCA cleaning process. First a 2 µm thick

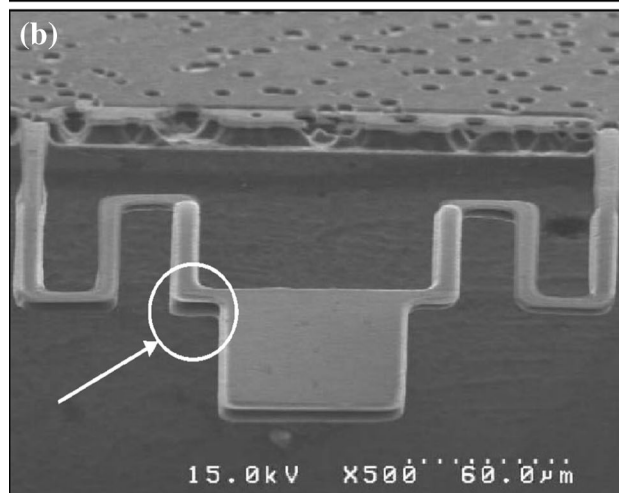
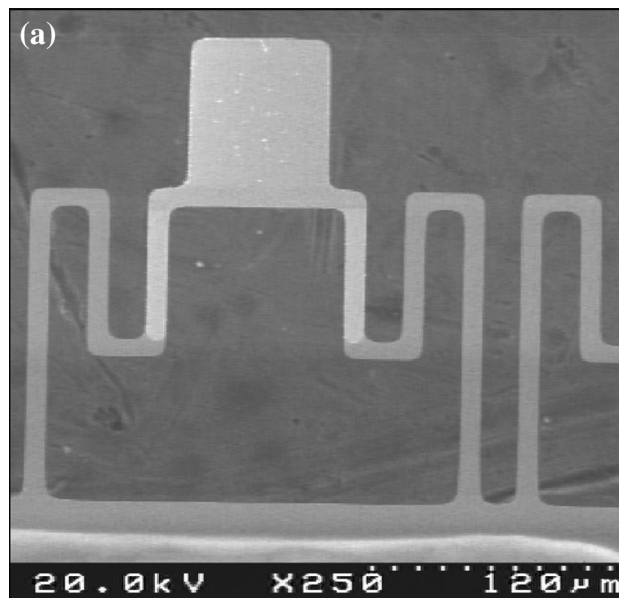


Fig. 8 *Top* view SEM images of the fabricated micro-cantilever detector. The structure is fully suspended and aluminum legs are visible. **b** *Front* of view SEM images of the fabricated microcantilever detector. The presence of double layer is clearly observed in this figure

silicon dioxide is thermally grown on double-side substrate by means of wet oxidation process, then 400 nm thick Cr layer is then evaporated on top of the SiO₂ on front side of wafer using thermal evaporation. This Cr layer is used for SiO₂ patterning and extra protection of SiO₂ during the subsequent etching of Si in TMAH. Cr deposition is followed by 1 h annealing at 400 °C at 5 sccm Argon flow pressure. As seen in part (c) of this figure, a square window is opened on the back side of SiO₂ using standard lithography process by buffered hydrofluoric acid (BOE) etching. Subsequently the silicon substrate is etched using commercially available TMAH (25 %, Merck, Germany) at 90 °C for 6 h to make 60 µm thin membrane (Brida et al. 2000). Double-side lithography is used to pattern the front

side and backside square windows. Cr is then etched by Ammonium Cerium (IV) Nitrate $((\text{NH}_4)_2\text{Ce}(\text{NO}_3)_6)$ diluted with DI water for 60 s. This step is shown in part (d) of Fig. 5.

Backside silicon substrate etching is again continued by immersion in TMAH (25 %) until red thin film membrane is observed. The SiO_2 layer is then removed completely using BOE for 40 min. This process is practiced because the previously grown SiO_2 had lost its quality during different thermal and chemical process. Following this step, Cr is removed completely by Cr etchant using aqueous $(\text{NH}_4)_2\text{Ce}(\text{NO}_3)_6$ for 60 s as shown in Fig. 5h. A fresh 1 μm thick silicon dioxide layer is then thermally grown on front-side substrate to make basic structure by the wet oxidation process, for 4 h at 1,050 $^\circ\text{C}$. The SiO_2 structure is then patterned on front-side of silicon substrate with photolithography technique employing wet etching technique by BOE etchant for 25 min. To finalize the fabrication process, a 200 nm thick Al layer is evaporated on the front side of wafer using thermal deposition on top of the SiO_2 to define bi-material. This layer is then patterned by a lift-off technique.

Then after, the Si substrate is etched using a silicon doped solution in TMAH (5 %) for 2 h at 80 $^\circ\text{C}$. The silicon doped solution in TMAH (5 %) is prepared by dilution of commercially available TMAH 25 wt% water solutions. Amorphous silicon (15 g/l) is then dissolved in TMAH (5 %) for Al passivation. Before immersion of substrate in the Si etchant, native oxide is removed by using Hydrofluoric acid (2 % HF) etchant for a short time and immediately rinsed in DI water to prevent damage on Al patterns (Biswas et al. 2006). (Please observe Fig. 5l). Finally, the detector is released in dual-doped TMAH using a low temperature wet release process. The substrate is immersed in DI water for 5 min to dilute the dual-doped TMAH. The substrate is again immersed for 5 min to another fresh DI water to insure that no residual TMAH is on the detector. Then, the substrate is immersed in acetone for 5 min to dissolve the DI water. The substrate is again immersed for 5 min to another fresh acetone to insure that the acetone and water are replaced completely. Next, the substrate is slowly released in the acetone. Releasing process is accomplished at room temperature, with no drying process to make sure that the structure is not damaged, and the substrate is vertically immersed and released in the dilution (Fig. 5m).

6 Experimental results

The following optical and electron microscopy images show the various steps which have been performed in the fabrication of these devices. Figure 6 shows the results of

back-side etching using TMAH etching process. A smooth bottom of the crater indicates the successful etching of the silicon without hillock formation. The collapsed edges of the etching crater are the masking layer which has been damaged during the handling for SEM specimen preparation.

Figure 7 shows an optical image of the device after aluminum patterning has been carried out. The difference in the color of the side-bars is due to the different materials used for these structures. Arrow in this figure points at bi-material regions.

Figure 8 shows the top and front views SEM images of the fabricated SiO_2/Al microcantilever uncooled IR detector, respectively. While in part (a) one can observe the free standing of the cantilever, the more detailed view of

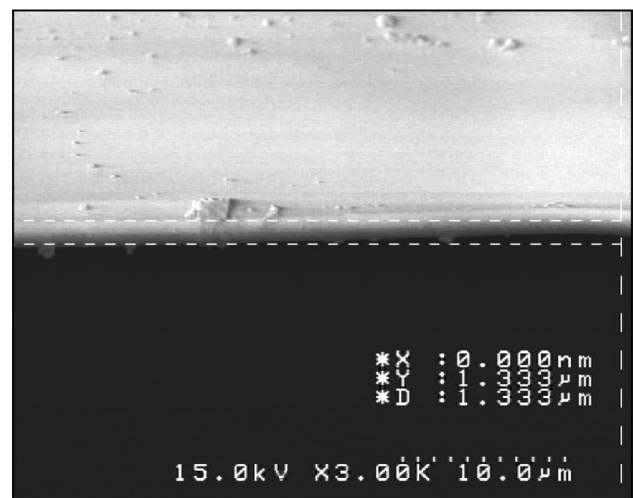


Fig. 9 SEM images of cross-section SiO_2 leg. The thickness of the layer is around 1.3 μm in accordance with the deposited oxide

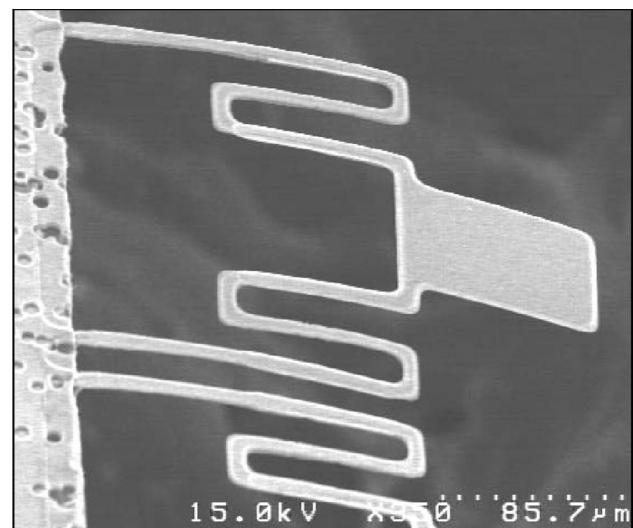


Fig. 10 Bending of detector due to changing of temperature. This is a suitable reaction of the sensor upon heating by an external signal

part (b) shows the formation of double-layered structure where two parallel plates are pointed at with an arrow.

Figure 9 shows the cross-section of SiO₂ leg. The thickness of the layer is found to be around 1.3 μm which is close to the original value set by the deposition of the oxide layer. And finally the bending of detector due to changing of temperature is shown in Fig. 10. In this figure, the fully suspended structure is bent upon exposure to an external thermal signal.

7 Conclusion

In this paper, a simple microfabrication process to fabricate a suspended Al/SiO₂ uncooled bi-material microcantilever IR detector using silicon bulk micromachining technology and wet releasing process has been introduced. Fabrication is formed by using the membrane structure. The process consists of four photolithographic processes with 3 masks. The main advantage of this fabrication process is that no sacrificial layer is used, and so the complexity of releasing sacrificial layer is avoided. It is shown that Al layer in this structure could be protected during Si etching process using dual-doped TMAH etchant. In addition, Al layer is also acting as a mirror for IR incident radiation in the absorbing area and as a result improves the IR absorption. Since, no etching hole is needed in this structure; the absorption is even more increased. It is also shown that using bi-material over the whole absorbing area as well as bi-material legs, helps to increase the displacement of microcantilever. The detector displacement is also maximized due to temperature variation and extension of the bi-material region to the IR absorber area.

References

- Biswas K, Das S, Maurya DK, Kal S, Lahiri SK (2006) Bulk micromachining of silicon in TMAH-based etchants for aluminum passivation and smooth surface. *Microelectron J* 37:321–327. doi:10.1016/j.mejo.2005.05.013
- Brida S, Faes A, Guarnieri V, Giacomozzi F, Margesin B, Paranjape M, Pignatelli GU, Zen M (2000) Microstructures etched in doped TMAH solutions. *Microelectron Eng* 53:547–551. doi:10.1016/j.mejo.2005.05.013
- Cao J, Chen Z, Lu W, Zhang Y, Lei K, Zhao B (2009) Design of readout circuit for microcantilever-based ripple uncooled infrared focal plane arrays. *Proceedings of SPIE, International Symposium on Photoelectronic Detection and Imaging* 7383: 73834J doi:10.1117/12.836710
- Cheng T, Zhang Q-C, Jiao B-B, Chen D-P, Wu X-P (2009) Analysis of optical readout sensitivity for uncooled infrared detector. *Chinese Phys Lett* 26(12):124206. doi:10.1088/0256-307X/26/12/124206
- Cheng G, Zhao Y, Dong L, Hui M, Yu X, Liu X (2013a) Short-wave infrared, medium-wave infrared, and long-wave infrared imaging study for optical readout microcantilever array infrared sensing system. *Opt Eng* 52(2):0264031–0264037. doi:10.1117/1.OE.52.2.026403
- Cheng G, Zhao Y, Dong L, Hui M, Yu X, Liu X (2013b) The tolerable target temperature for bi-material microcantilever array infrared imaging. *Opt Laser Technol* 45:545–550. doi:10.1016/j.optlastec.2012.05.034
- Correa M, Hermosilla G, Verschae R, Ruiz-del-Solar J (2012) Human detection and identification by robots using thermal and visual information in domestic environments. *J Intell Robot Syst* 66:223–243. doi:10.1007/s10846-011-9612-2
- Datskos PG, Lavrik NV, Rajic S (2004) Performance of uncooled microcantilever thermal detectors. *Rev Sci Instrum* 75:1134–1148. doi:10.1063/1.1667257
- Dobrzafiski L, Nossarzewska-Odowska E, Nowak Z, Piotrowski J (1997) Micromachined silicon bolometers as detectors of soft X-ray, ultraviolet, visible and infrared radiation. *Sens Actuators A* 60:154–159. doi:10.1016/S0924-4247(97)01512-4
- Dong F, Zhang Q, Chen D, Pan L, Guo Z, Wang W, Duan Z, Wu X (2007) An uncooled optically readable infrared imaging detector. *Sens Actuators A* 133:236–242. doi:10.1016/j.sna.2006.04.031
- Fujitsuka N, Sakata J, Miyachi Y, Mizuno K, Ohtsuka K, Taga Y, Tabata O (1998) Monolithic pyroelectric infrared image sensor using PVDF thin film. *Sens Actuators A* 66:237–243. doi:10.1109/sensor.1997.635451
- Gray GJ, Aouf N, Richardson M, Butters B, Walmsley R (2013) Countermeasure effectiveness against an intelligent imaging infrared anti-ship missile. *Opt Eng* 52(2):026401–026410. doi:10.1117/1.OE.52.2.026401
- Grbovic D, Lavrik NV, Rajic S, Datskos PG (2008a) Arrays of SiO₂ substrate-free micromechanical uncooled infrared and terahertz detectors. *J Appl Phys* 104:05450801–05450807. doi:10.1063/1.2959574
- Grbovic D, Rajic S, Lavrik NV, Datskos PG (2008b) Progress with MEMS based UGS (IR/THz). *Proceedings of SPIE, Unattended Ground, Sea, and Air Sensor Technologies and Applications X* 6963: 69631701–69631711 doi:10.1117/12.786633
- Grbovic D, Karunasiri G, Rajic S, Datskos PG (2009) Fabrication of Bi-material MEMS detector arrays for THz imaging. *Proceedings of SPIE, Terahertz Physics, Devices, and Systems III* 7311: 7311081–7311087 doi:10.1117/12.818317
- Hunter SR, Maurer G (2006) High sensitivity Uncooled microcantilever infrared imaging arrays. *Proceedings of SPIE, Infrared Technology and Applications XXXII* 6206: 62061j1–62061j13. doi:10.1117/12.726316
- Hunter SR, Maurer G (2007) High sensitivity 25 μm and 50 μm pitch microcantilever IR imaging arrays. *Proceedings of SPIE, Infrared Technology and Applications XXXIII* 6542:65421F1–65421F13. doi:10.1117/12.664727
- Jiao B, Chen D, Li C, Shi S, Ye T, Zhang Q, Guo Z, Dong F, Miao Z (2006) Design of a novel uncooled infrared focal plane array. *Proceedings of the 1st IEEE International Conference on Nano/Micro Engineered and Molecular Systems* pp 430–433. doi:10.1109/NEMS.2006.334792
- Kruse PW (1995) A comparison of the limits to the performance of thermal and photon detector imaging arrays. *Infrared Phys Technol* 36(5):869–882. doi:10.1016/1350-4495(95)00014-p
- Kruse PW (1996) *Uncooled infrared imaging arrays and systems*. vol. 47
- Kwon IW, Kim JE, Hwang CH, Kim TK, Lee YS, Lee HC (2007) A high fill-factor uncooled infrared detector with thermo-mechanical bimaterial structure. *Proceedings of SPIE, Infrared Technology and Applications XXXIII* 6542: 65421O1–65421O10 doi:10.1117/12.719207
- Kwon IW, Kim JE, Hwang CH, Kim TK, Lee YS, Lee HC (2008) A high fill-factor uncooled infrared detector with low noise characteristic. *Proceedings of SPIE, Infrared Technology and*

- Applications XXXIV 6940:694014 01-694014 01. doi: [10.1117/12.780506](https://doi.org/10.1117/12.780506)
- Kwon IW, Son HJ, Kim DS, Hwang CH, Lee YS, Yu BG, Lee HC (2009) A cantilever-type uncooled infrared detector with high fill-factor and low-noise characteristic. *Electron Device Lett* 30:635–637. doi:[10.1109/LED.2009.2013221](https://doi.org/10.1109/LED.2009.2013221)
- Li B (2004) Design and simulation of an uncooled double-cantilever micro bolometer with the potential for ~mK NETD. *Sens Actuators A* 112:351–359. doi:[10.1016/j.sna.2004.01.031](https://doi.org/10.1016/j.sna.2004.01.031)
- Li Y, Zheng Q, Hu Y, Xu Y (2011) Micromachined piezoresistive accelerometers based on an asymmetrically gapped cantilever. *J Microelectromech Syst* 20(1):83–94. doi:[10.1109/JMEMS.2010.2100024](https://doi.org/10.1109/JMEMS.2010.2100024)
- Oh SJ, Huh Y-M, Suh J-S, Choi J, Haam S, Son J-H (2012) Cancer diagnosis by terahertz molecular imaging technique. *J Infrared Milli Terahz Waves* 33:74–81. doi:[10.1007/s10762-011-9847-9](https://doi.org/10.1007/s10762-011-9847-9)
- Razeghi M, Haddadi A, Hoang AM, Huang EK, Chen G, Bogdanov S, Darvish SR, Callewaert F, McClintock R (2013) Advances in antimonide-based type-II super lattices for infrared detection and imaging at canter for quantum devices. *Infrared Phys Technol*. doi:[10.1016/j.infrared.2012.12.008](https://doi.org/10.1016/j.infrared.2012.12.008)
- Schieferdecker J, Quad R, Holzenkampfer E, Schulze M (1995) Infrared thermopile sensors with high sensitivity and very low temperature coefficient. *Sens Actuators A* 46(47):422–427. doi: [10.1016/0924-4247\(94\)00934-A](https://doi.org/10.1016/0924-4247(94)00934-A)
- Su B, Duan G (2011) A high sensitivity THz Detector. *Proceedings of SPIE, International Symposium on Photoelectronic Detection and Imaging: Terahertz Wave Technologies and Applications* 8195: 81951K1–81951K7 doi:[10.1117/12.900992](https://doi.org/10.1117/12.900992)
- Szentpali B, Matyi G, Furjes P, Laszlo E, Battistig G, Barsony I, Karolyi G, Berceli T (2012) Thermopile-based THz antenna. *Microsyst Technol* 18:849–856. doi:[10.1007/s00542-011-1387-7](https://doi.org/10.1007/s00542-011-1387-7)
- Vigni ML, Cocchi M (2013) Near infrared spectroscopy and multivariate analysis to evaluate wheat flour doughs leavening and bread properties. *Anal Chim Acta* 764:17–23. doi:[10.1016/j.aca.2012.12.018](https://doi.org/10.1016/j.aca.2012.12.018)
- Wang W, Upadhyay V, Munoz C, Bumgarner J, Edwards O (2006) FEA Simulation, design and fabrication of uncooled MEMS capacitive thermal detector for infrared FPA imaging. *Proceedings of SPIE, Infrared Technology and Applications XXXII* 6206: 62061L1–62061L12. doi:[10.1117/12.665080](https://doi.org/10.1117/12.665080)
- Wang B, Lai J, Zhao E, Hu H, Chen S (2012) Research on VOx uncooled infrared bolometer based on porous silicon. *Front Optoelectron* 5(3):292–297. doi:[10.1007/s12200-012-0224-7](https://doi.org/10.1007/s12200-012-0224-7)
- Wang B, Lai J, Li H, Hu H, Chen S (2013) Nanostructured vanadium oxide thin film with high TCR at room temperature for microbolometer. *Infrared Phys Technol* 57:8–13. doi:[10.1016/j.infrared.2012.10.006](https://doi.org/10.1016/j.infrared.2012.10.006)
- Xu Z, Yan D, Xiao D, Yu P, Zhu J (2012) Temperature field and residual stress analysis of multilayer pyroelectric thin film. *Ceram Int* 38:981–985. doi:[10.1016/j.ceramint.2011.08.019](https://doi.org/10.1016/j.ceramint.2011.08.019)
- Zhao Y (2002) Optomechanical uncooled infrared imaging system. Dissertation, UC, Berkeley
- Zhao Y, Mao M, Horowitz R, Majumdar A, Varesi J, Norton P, Kitching J (2002) Optomechanical uncooled infrared imaging system: design, microfabrication, and performance. *J Microelectromech Syst* 11:136–146. doi:[10.1109/84.993448](https://doi.org/10.1109/84.993448)
- Zhao A-D, Zheng Y-J, Yu X-M (2012) Imaging and characteristics of a bimaterial microcantilever FPA fabricated using bulk silicon processes. *Chinese Phys Lett* 29(5):058502. doi:[10.1088/0256-307X/29/5/058502](https://doi.org/10.1088/0256-307X/29/5/058502)
- Zhu D-Q, Shen W-T, Cai G-B, Ke W-N (2013) Numerical simulation and experimental study of factors influencing the optical characteristics of a spatial target. *Appl Therm Eng* 50:749–762. doi:[10.1016/j.applthermaleng.2012.08.017](https://doi.org/10.1016/j.applthermaleng.2012.08.017)